Nano Research

Open Access

Research Article

# Regulating the oxygen-atom configuration of carbon anode enabling extremely fast-charging potassium-ion hybrid capacitors

Daping Qiu[1], Yuehui Wang[1], Lulu Zhang[1], Hang Lei[1], Haizhou Ying[1], Jin Niu[2], Min Li[2], Xuelin Yang[1,3] ✉, Feng Wang[2] ✉, and Ru Yang[2] ✉

[1] *Hubei Provincial Collaborative Innovation Center for New Energy Microgrid, College of Electrical Engineering and New Energy, China Three Gorges University, Yichang 443002, China*
[2] *State Key Laboratory of Chemical Resource Engineering, Laboratory of Electrochemical Process and Technology for Materials, Beijing University of Chemical Technology, Beijing 100029, China*
[3] *College of Materials and Chemical Engineering, China Three Gorges University, Yichang 443002, China*

**Cite this article:** *Nano Research*, **2025**, *18*, 94907033. https://doi.org/10.26599/NR.2025.94907033

**ABSTRACT:** Metal-ion hybrid capacitors, such as potassium-ion hybrid capacitors (PIHCs), are regarded as promising fast-charging energy storage devices. However, the kinetics mismatch between the battery anode and the capacitive cathode restricts their fast-charging performance. Precisely constructing carbon anodes with enhanced kinetics is an innovative approach to address this challenge. Herein, using epigallocatechin gallate with high oxygen content as the precursor, oxygen-enriched carbon materials (OEC) with tunable C=O content are successfully synthesized. Effortlessly, the C=O content of OEC is regulated by adjusting the pyrolysis temperature. Serving as an anode for PIHCs, OEC-600 with the highest C=O content exhibits an attractive fast-charging specific capacity of 135.2 mAh·g$^{-1}$ at 20 A·g$^{-1}$, along with a superior fast-charging cycling stability. Combining theoretical calculations, comprehensive kinetics analysis and *in-situ* Raman, the positive effects of C=O on the potassium storage capability and reversibility of OEC-600 are revealed. Consequently, PIHCs assembled based on an OEC-600 anode deliver impressive energy/power density of 145.1 Wh·kg$^{-1}$/45.9 kW·kg$^{-1}$ and superior fast-charging cycling stability with 87.5% of capacity retention over 20,000 cycles at 5 A·g$^{-1}$. This work is anticipated to provide an optional design concept toward the carbon anode for fast-charging PIHCs.

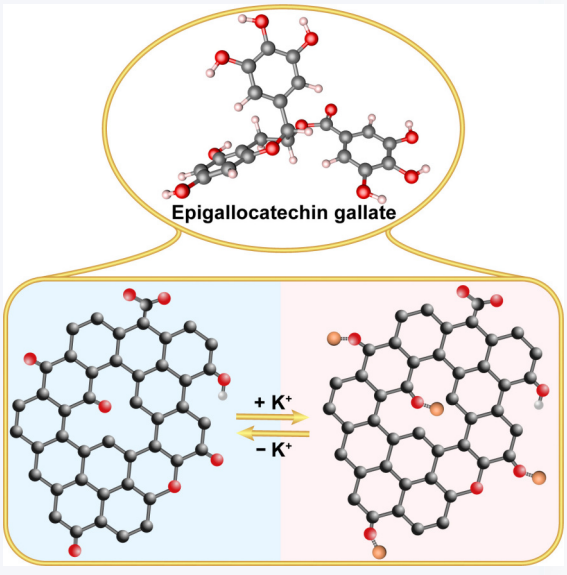


**KEYWORDS:** carbon, anode, oxygen, epigallocatechin gallate, potassium-ion hybrid capacitor

## 1 Introduction

With the continuous promotion of global carbon neutrality, there is an urgent demand to accelerate the electrification of vehicles [1–3]. However, in comparison to gasoline-powered vehicles, the recharging rate of electric vehicles (EVs) is extremely sluggish (typically up to half an hour or even one hour), which has been considered a barrier to further expansion of their market [3–5]. In this context, developing the next-generation of energy storage technologies with extremely fast-charging capabilities is an urgent task to ensure that EVs overcome the barrier. Alkali metal-ion batteries (AIBs), typically represented by lithium-ion batteries, have been acknowledged as the most compatible energy storage technology for EVs power supplies over the past decade [6]. However, due to the sluggish battery reactions involved in cathode and anode (intercalation, conversion, alloying, etc.), it is almost impossible to achieve extremely fast-charging based on traditional AIBs architecture. Tremendous attempts have been devoted to optimize the structure of electrode materials and customize the electrolytes to enhance the fast-charging performance of AIBs

**Received:** July 22, 2024; **Revised:** September 3, 2024
**Accepted:** September 12, 2024

✉Address correspondence to Xuelin Yang, xlyang@ctgu.edu.cn; Feng Wang, wangf@mail.buct.edu.cn; Ru Yang, ruyang@mail.buct.edu.cn

[7–9]. However, these attempts either compromise the energy density of AIBs or come at a high cost. Metal-ion hybrid capacitors (MIHCs), an emerging energy storage architecture that integrates a high energy density battery anode and a high power density capacitive cathode, are considered promising candidates for the next-generation of fast-charging energy storage devices [10, 11].

Potassium-ion hybrid capacitors (PIHCs) have garnered widespread interest as cost-effective MIHCs [10]. Since the prototype was first proposed in 2017, the development of PIHCs has reached several witnessed milestones [12–16]. For example, Liu et al. proposed a graphite anode without preactivation processes based on the cointercalation mechanism of diglyme-solvated $K^+$ and successfully assembled PIHCs with a power density up to 15,887 $W{\cdot}kg^{-1}$ [13]; Li et al. successfully assembled 1 Ah soft-package PIHCs based on N-CNT@MC cathode (CNT: carbon nanotube and MC: mesoporous carbon) and MnO@CNTs anode for the first time and achieved an energy density of 140 $Wh{\cdot}kg^{-1}$ with a full charge of 6 min [14]; in addition, our group has comprehensively investigated the modulation mechanism of binders on the potassium storage performance of carbon anodes for PIHCs, thus proposing candidate binders [15]. However, it is a grim point that energy density is the central concern in most reports, yet power density is frequently disregarded. Therefore, the current PIHCs are still "battery" devices with inferior energy density, rather than hybrid energy storage devices that integrate high energy and high power. Hence, it is highly in demand to develop advanced strategies to construct fast-charging PIHCs.

Drawing on past research experience on PIHCs, the most critical factor restricting the fast-charging performance of PIHCs is the kinetics mismatch between the battery anode and the capacitive cathode, or the sluggish potassium storage kinetics of the battery anode [11, 17]. Among the various types of battery anodes, carbon materials are regarded as the most promising candidates for fast-charging anodes due to their considerable specific capacity, competitive rate capability and excellent cycling stability [18–20]. Unfortunately, even so, the potassium storage kinetics of carbon anodes still trail far behind those of capacitive cathodes. To address this challenge, structural modulations, such as pore structure optimization, graphitization degree regulation and heteroatom doping, are alternative strategies [21–23]. Among them, heteroatom doping is one of the most universal and widespread strategies. On the one hand, heteroatoms such as O, N, S and P can effectively enhance the potassium storage kinetics of carbon anodes by providing unpaired electrons, distorting the carbon framework and inducing electron delocalization, etc.; on the other hand, these heteroatoms can contribute the slope capacity at high voltage [23]. Of them, O, the most common heteroatom derived from the precursor, is the cheapest and most easily doped one [24, 25]. However, O-doping suffers from two severe challenges: (1) It is difficult to selectively dope oxygen-containing functional groups (OFGs) with electrochemical activity due to the diversity of OFGs; (2) the synthesis of carbon anodes involves high temperature carbonization procedure, resulting in difficulty in retaining OFGs.

To address the above issues, we have selected epigallocatechin gallate (EGCG, $C_{22}H_{18}O_{11}$), one of the green tea polyphenols with a high oxygen content (38.4 at.%), to synthesize oxygen-enriched carbon materials (OEC) for fast-charging PIHCs. EGCG self-oxidizes and cross-links with $Ca^{2+}$ in alkaline solution to generate ultra-fine nanogel particles, following with the formation of OEC with high C=O content in the pyrolysis step. In this procedure, the C=O content of OEC can be easily regulated by adjusting the pyrolysis temperature. As a result, OEC-600 (pyrolyzed at 600 °C) with the highest C=O content exhibits attractive fast-charging specific capacity and cycling stability in K-half cells. Furthermore, combining theoretical calculations, comprehensive kinetics analysis and *in-situ* Raman, we have revealed the nature of the attractive fast-charging potassium storage capability of OEC-600. Finally, the OEC-600 based PIHCs deliver impressive energy/power density (145.1 $Wh{\cdot}kg^{-1}$/45.9 $kW{\cdot}kg^{-1}$) and fast-charging cycling stability (87.5% of capacity retention over 20,000 cycles at 5 $A{\cdot}g^{-1}$), validating the excellent fast-charging potassium storage potential of OEC-600.

## 2 Experimental

### 2.1 Materials preparation

4 g of EGCG (Aladdin) and 4.44 g of anhydrous $CaCl_2$ (Aladdin) were dissolved in 200 mL of deionized water successively to prepare solution A; 4.2 g of anhydrous $Na_2CO_3$ (Aladdin) was dissolved in 50 mL of deionized water to prepare solution B. Then, solution B was added dropwise to solution A with a rate of 2 $mL{\cdot}min^{-1}$ under vigorous stirring and stirring was continued for 30 min after solution B was completely added. The synthesized purple precipitate was collected by centrifugation (7000 $r{\cdot}min^{-1}$), washed three times with deionized water and ethanol and then freeze-dried in a freeze drier for 24 h. Subsequently, the collected purple powder was placed into a tube furnace for carbonization for 2 h in Ar atmosphere. Finally, the carbonized residue was stirred in 1 M HCl for 2 h to remove the hard template, washed with deionized water until neutral and dried at 80 °C for 12 h in a vacuum oven. The samples were named as OEC-$x$ ($x$ = carbonization temperature). EC-600 was obtained by directly carbonizing EGCG under the same conditions. To determine the optimal precursor component, precursors with different EGCG contents were carbonized at 600 °C to obtain OEC-0.5, OEC-2 and OEC-3 (mass ratio of EGCG to $CaCO_3$, $m$(EGCG)/$m$($CaCO_3$) = 0.5, 2, 3).

### 2.2 General characterization

The graphitization degree was determined by X-ray diffractometer (SmartLab, Rigaku) and Raman spectrometer (DXR2, Thermo Fisher). The morphology and microstructure information were acquired on scanning electron microscopy (SEM, GeminiSEM 300, ZEISS) and transmission electron microscopy (TEM, JEM-F200, JEOL). X-ray photoelectron spectrometer (AXIS Supra, SHIMADZU) and Fourier transform infrared (FTIR) spectrometer (Nicolet iS 10, Thermo Fisher) were applied to investigate the atomic configurations of carbon framework. Element analyzer (UNICUBE, Elementar) was used to quantify the element content and thermo gravimetric analyzer (STA 449 F5, NETZSCH) was performed to simulate the carbonization process. $N_2$ adsorption–desorption tests were performed on a surface area and porosity analyzer (ASAP 2460, Micromeritics) and the specific surface area and porosity were calculated based on Brunauer–Emmett–Teller theory and density functional theory, respectively.

### 2.3 Electrochemical measurements

The preparation process of the working electrodes and the assembly process of the K-half cell are the same as our previous work [15]. Glass fibers (GF/A, Whatman) and 1 M KFSI in ethylene carbonate (EC):diethyl carbonate (DEC) (1:1 in volume) were selected as separator and electrolyte, respectively. PIHCs were assembled with

prepotassiated OEC-600 (three times at 0.1 $A \cdot g^{-1}$) as anode and EGCG-based hierarchical porous carbon sphere (HPCS) as cathode. Galvanostatic charge–discharge (GCD) and galvanostatic intermittent titration technique (GITT) tests were finished in the cell test system (CT-4008Tn, NEWARE). Cyclic voltammetry (CV) and *in-situ* electrochemical impedance spectroscopy (EIS) tests were performed with an electrochemical workstation (VSP-300, BioLogic). The calculation method for the energy density and power density of PIHCs refers to our previous work [15].

### 2.4 Calculation details

The calculation of electrostatic potential (ESP) for oxygen-enriched carbon and defect carbon adopted the B3LYP function implemented in Gaussian 16 [26]. The ESP surfaces images were drawn using the Multiwfn 3.8 program [27].

## 3 Results and discussion

OEC, were synthesized by pyrolysis of auto-oxidation EGCG, as illustrated in Fig. 1(a). Briefly, EGCG can auto-oxidize (Fig. S1 in the Electronic Supplementary Material (ESM)) and cross-link with $Ca^{2+}$ in alkaline solution, resulting in the generation of ultra-fine nanogel particles (Fig. S2 in the ESM) [28]; then, after high temperature pyrolysis and hard template ($CaCO_3$) removal, OEC-600 (pyrolysis at 600 °C) with multi-cavity nanosphere morphology (Figs. 1(c) and 1(d)) can be collected. Notably, the effect of pyrolysis temperature on the morphology of the products was evaluated and the morphologies of OEC-700, OEC-800 and OEC-900 (Fig. S3 in the ESM) are generally consistent with that of OEC-600. In addition, as displayed in Fig. S4 in the ESM, EC-600 with the absence of hard template presents a densely stacked bulk morphology. To confirm the carbonization temperature of auto-oxidation EGCG, thermogravimetric analysis (TG) and *ex-situ* X-ray diffraction (XRD) were performed. As shown in Fig. S5 in the ESM, the precursor has three obvious weight loss stages in the range of 70–170, 200–350 and 575–750 °C, where the first belongs to the volatilization of adsorbed water, the second is assigned to the degradation reaction of auto-oxidation EGCG and the last is the carbonization step and the decomposition of $CaCO_3$. Furthermore, as observed from Fig. 1(b), the XRD patterns of products with different pyrolysis temperatures exhibit visible differences. Specifically, the XRD patterns of the pyrolysis products at 500 and 600 °C are indexed to $CaCO_3$, but when the temperature rises to 700 °C, CaO is generated and the diffraction peaks of $CaCO_3$ almost disappear [29, 30]. It means that the decomposition reaction of $CaCO_3$ in the third weight loss stage occurs above 600 °C and the carbonization temperature of auto-oxidation EGCG is ~ 575 °C. Taking OEC-600 as a typical example, its microstructure was

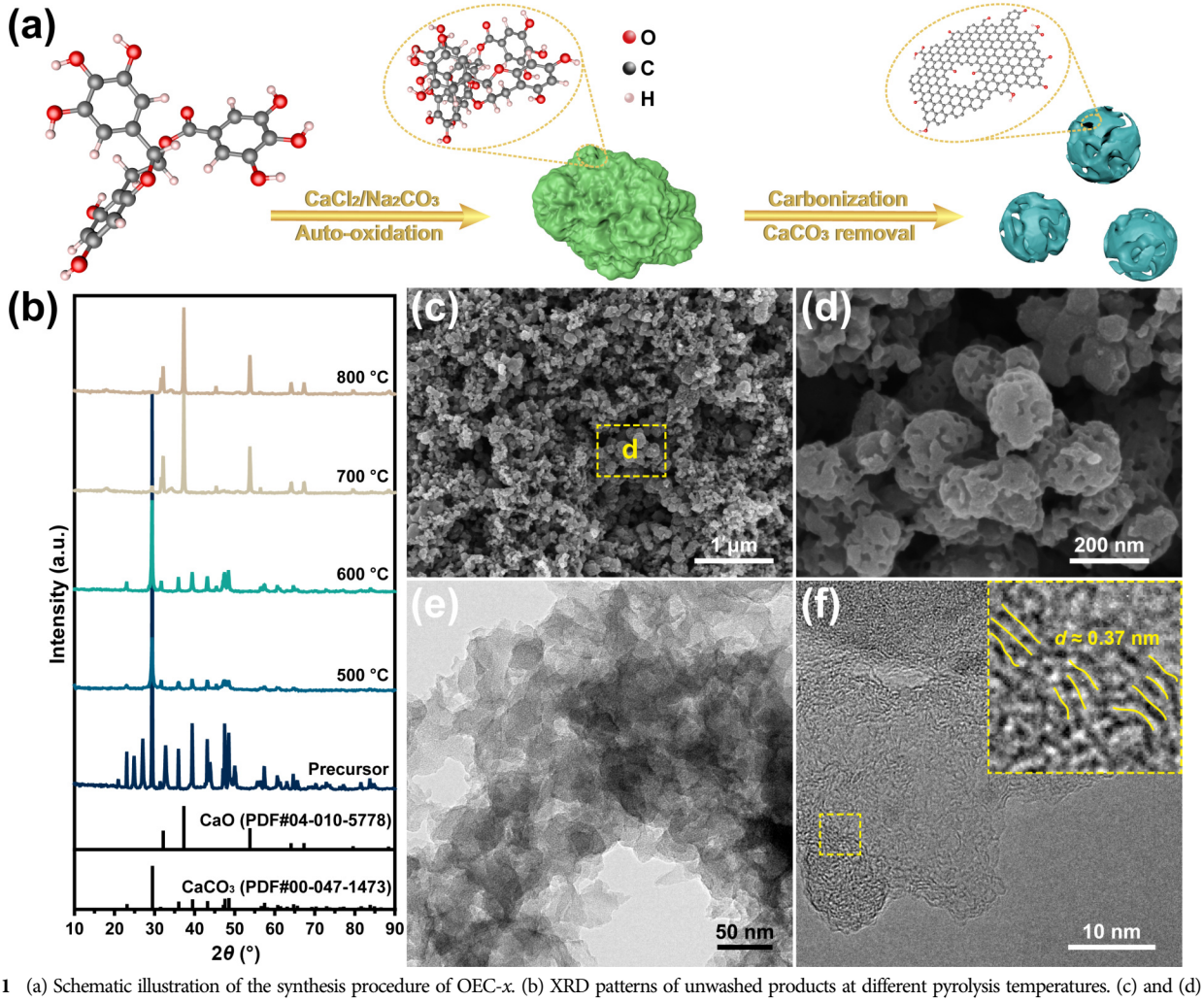


**Figure 1** (a) Schematic illustration of the synthesis procedure of OEC-*x*. (b) XRD patterns of unwashed products at different pyrolysis temperatures. (c) and (d) SEM images; (e) and (f) TEM images (insets of (f) are the calculated interlayer spacing and enlarged image of the yellow dotted rectangular area) of OEC-600.

investigated using TEM. As exhibited in Fig. 1(e), the OEC-600 presents a multi-cavity microstructure with interconnected nanoflakes. Further, the high-resolution TEM image (Fig. 1(f)) discloses the amorphous crystalline nature of OEC-600 and the carbon interlayer spacing of OEC-600 calculated based on the lattice fringes is ~ 0.37 nm. In addition, energy dispersive spectroscopy elemental mapping (Fig. S6 in the ESM) demonstrates the homogeneous distribution of C and O.

As shown in Fig. 2(a), a broad peak near 23° ((002) plane of graphite) and a faintly visible peak near 43° ((100) plane of graphite) can be observed from the XRD patterns of OEC-*x* (*x* = 600, 700, 800 and 900), which reveals that they are typical amorphous carbon [15, 31]. Raman spectroscopy was applied to distinguish the graphitization degree of OEC-*x*. As observed in Fig. 2(b), the Raman spectra are fitted to four bands: the T-band at ~ 1200 $cm^{-1}$ ($sp^3$-boned carbon atoms/heteroatoms), the D-band at ~ 1350 $cm^{-1}$ (C–C vibrations in disordered graphitic lattices with $A_{1g}$ symmetry), the D"-band centered at ~ 1500 $cm^{-1}$ (in-plane non-hexagonal carbon atoms) and the G-band at ~ 1580 $cm^{-1}$ (the ideal C–C vibrations in graphitic lattice with $E_{2g}$-symmetry) [32, 33]. Among them, the area ratio of D-band to G-band ($A_D/A_G$) is a reliable indicator for evaluating the graphitization degree of carbon materials and the area ratio of T-band to G-band ($A_T/A_G$) can be used to estimate the content of C atoms bonded with heteroatoms [33, 34]. As a result, the $A_D/A_G$ indicators for OEC-600, OEC-700, OEC-800 and OEC-900 are 1.73, 1.9, 1.85 and 1.8, respectively. In general, a higher carbonization temperature means a higher graphitization degree of carbon material. However, the $CO_2$ decomposed from $CaCO_3$ in the range of 600–700 °C has an etching effect on the carbon framework, resulting in a lower graphitization degree of OEC-700 compared to OEC-600 [35]. In addition, with the increase of carbonization temperature, the $A_T/A_G$ indicator of OEC-*x* exhibits a downward trend (from 0.76 to 0.45), suggesting that the content of oxygen-containing functional groups is negatively correlated with the carbonization temperature.

To confirm the atomic configurations of C and O, X-ray photoelectron spectroscopy (XPS) tests were conducted. The deconvoluted C 1s spectra of OEC-*x* are shown in Fig. S7 in the ESM, where the peaks of C=C/C–C, C–O and C=O can be identified [36]. It is obvious that the relative contents of the above three are different in each sample. Further, as displayed in Fig. 2(c), the O 1s spectra of OEC-*x* were deconvolved into C=O (~ 531.7 eV), C–O (~ 532.8 eV) and O=C–O (~ 534.0 eV) [36–38]. Notably, the relative content of C=O (the relative contents of C=O for OEC-600, OEC-700, OEC-800 and OEC-900 are 80.2%, 70.6%, 61.3% and 59.4%, respectively) is negatively correlated with the carbonization temperature, which suggests that C=O is unstable at high carbonation temperature. Combined with elemental analysis, the contents of O and C=O were quantified and the results are shown in Fig. 2(d). Whether it is O or C=O, the content decreases steadily with the increase of carbonization temperature. In addition, this fact can be further confirmed by the Fourier transform infrared spectra of OEC-*x* (Fig. S8(a) in the ESM). Surprisingly, even for partially carbonized OEC-500, its O and C=O content still follows this pattern (Fig. S9 in the ESM). It is worth noting that some pioneering work has demonstrated that C=O can reversibly store alkali metal-ions [24]. The evolution trend of the pore structure of OEC-*x* was analyzed with $N_2$ adsorption–desorption. As shown in Fig. S8(b) in the ESM, typical type I/VI isotherms can be observed, which indicates the hierarchical porous structure of OEC-*x* [39]. It is worth mentioning that, with the increase of carbonization temperature, there is a considerable difference in the adsorption volume of OEC-*x* at low relative pressure and medium relative pressure. To explain this phenomenon, the pore structure parameters are presented (Fig. S8(c) and Table S1 in the ESM). Specifically, first, the micropore volume of OEC-600 (0.174 $cm^3 \cdot g^{-1}$) is much lower than that of other samples (0.261, 0.232 and 0.246 $cm^3 \cdot g^{-1}$ for OEC-700, OEC-800 and OEC-900, respectively), which is attributed to the etching effect of $CO_2$ decomposed from $CaCO_3$; second, with the increase of carbonization temperature, the mesopore volume of OEC-*x* gradually rises (from 0.224 to 0.426 $cm^3 \cdot g^{-1}$), which is probably the synergistic effect of the oxygen

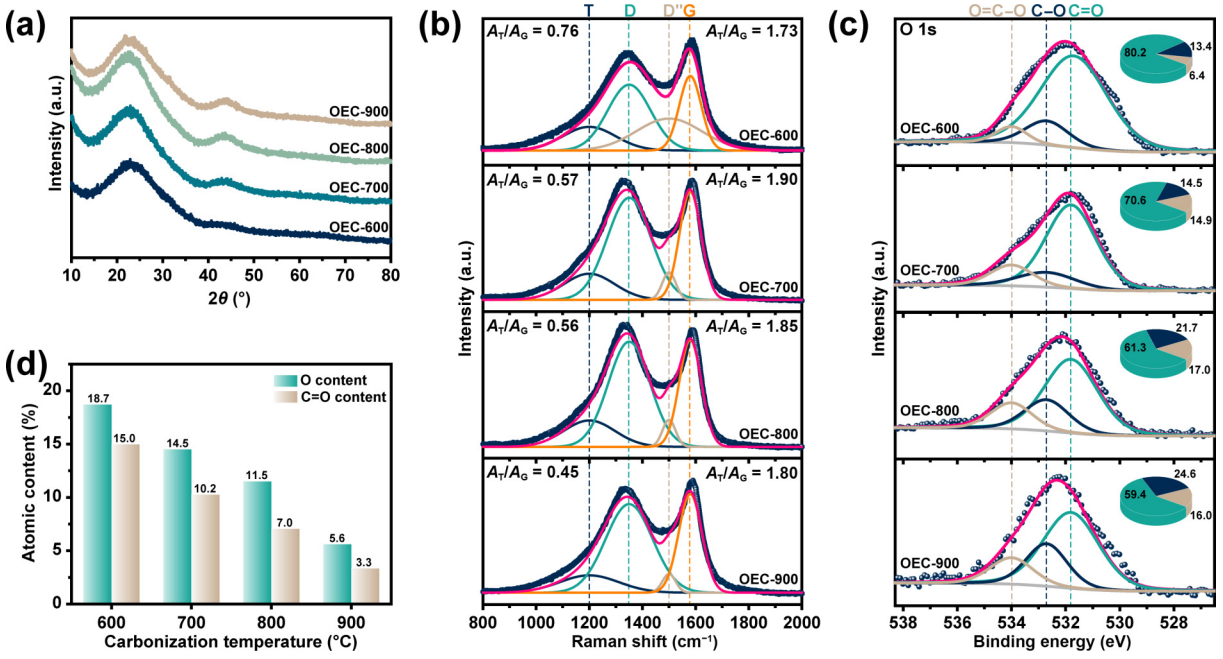


**Figure 2** (a) XRD patterns; (b) Raman spectra; (c) deconvolution O 1s spectra (insets are the relative content of oxygen-containing functional groups); (d) atomic content of O and C=O of OEC-*x*.

removal and $CO_2$ etching. Briefly, the carbonization temperature is a key controlling factor for the intrinsic structure of OEC-*x*, especially for the oxygen content and pore structure of OEC-*x*.

The potassium storage performance of OEC-*x* was comprehensively assessed in K-half cells. As shown in Fig. 3(a), the initial CV curve of OEC-600 demonstrates broad and intense irreversible reduction peaks in the low-voltage region, which are ascribed to the generation of a solid electrolyte interface (SEI) layer and the irreversible potassium storage [34]. The GCD curves of OEC-*x* for the initial three cycles at 0.1 $A{\cdot}g^{-1}$ are shown in Fig. 3(b) and Fig. S10 in the ESM, where the reversible specific capacity/initial Coulombic efficiency (CE) of OEC-600, OEC-700, OEC-800 and OEC-900 are 417.5 $mAh{\cdot}g^{-1}$/34.8%, 288.1 $mAh{\cdot}g^{-1}$/33.0%, 270.2 $mAh{\cdot}g^{-1}$/20.4% and 193.3 $mAh{\cdot}g^{-1}$/15.3%, respectively. It is evident that OEC-600 with the highest C=O content exhibits the most competitive reversible specific capacity and initial CE. Notably, the trend of the reversible specific capacity of OEC-*x* at the third cycle (shown in Fig. S11(a) in the ESM) with carbonization temperature is similar to that of C=O (Fig. 3(c)), which implies that C=O has a positive effect on the potassium storage performance of OEC-*x*. To validate the potassium storage capability of C=O, OEC-600 was calcined in an $Ar/H_2$ atmosphere to yield an oxygen-containing functional groups absent sample (OEC-600-$H_2$). As a consequence, the initial reversible specific capacity of OEC-600-$H_2$ at 0.1 $A{\cdot}g^{-1}$ drops to 336.1 $mAh{\cdot}g^{-1}$ (Fig. S11(b) in the ESM). Moreover, as can be seen in Fig. 3(d), compared to OEC-600, the specific capacity loss of OEC-600-$H_2$ is in the high-voltage region. It is well known that the reaction potential of C=O with alkali metal-ions is in this region, which determines that C=O can effectively participate in the potassium storage process of OEC-*x* [25]. The rate capabilities of OEC-*x* are shown in Fig. 3(e) and Fig. S12(a) in the ESM, where OEC-600 demonstrates attractive reversible specific capacities at various current densities. In particular, at an ultra-high current density of 20 $A{\cdot}g^{-1}$, OEC-600 achieves a reversible specific capacity of 135.2 $mAh{\cdot}g^{-1}$ with an extremely short discharge time of 27 s. Another point worth noting is that the trend of the reversible specific capacity of OEC-*x* with carbonization temperature at 0.5 $A{\cdot}g^{-1}$ (Fig. 3(c)) is closer to that of C=O than at 0.1 $A{\cdot}g^{-1}$. This fact reveals that C=O plays a crucial role in the fast-charging potassium storage process of OEC-*x*. In addition to attractive rate capability, OEC-600 shows superior cycling stability, as presented in Fig. 4(f) and Fig. S12(b) in the ESM. Specifically, the reversible specific capacity of OEC-600 after 100 cycles at 0.1 $A{\cdot}g^{-1}$ is 312.1 $mAh{\cdot}g^{-1}$; OEC-600 maintains 221.1 $mAh{\cdot}g^{-1}$ after 2000 cycles at a fast-charging current density of 2 $A{\cdot}g^{-1}$. In addition, OEC-500 (partially carbonized sample, Fig. S13 in the ESM) and EC-600 (Fig. S14 in the ESM) lag far behind OEC-600 in terms of initial CE, rate capability and cycling stability. Given the crucial role of C=O in the fast-charging potassium storage process of OEC-*x*, the superior cycling stability of OEC-600 at fast-charging current density is probably related to the high potassium storage reversibility of C=O. In short, benefiting from the fast potassium storage kinetics and high potassium storage reversibility of C=O (Fig. 3(g)), OEC-600 exhibits superior fast-charging specific capacity and fast-charging

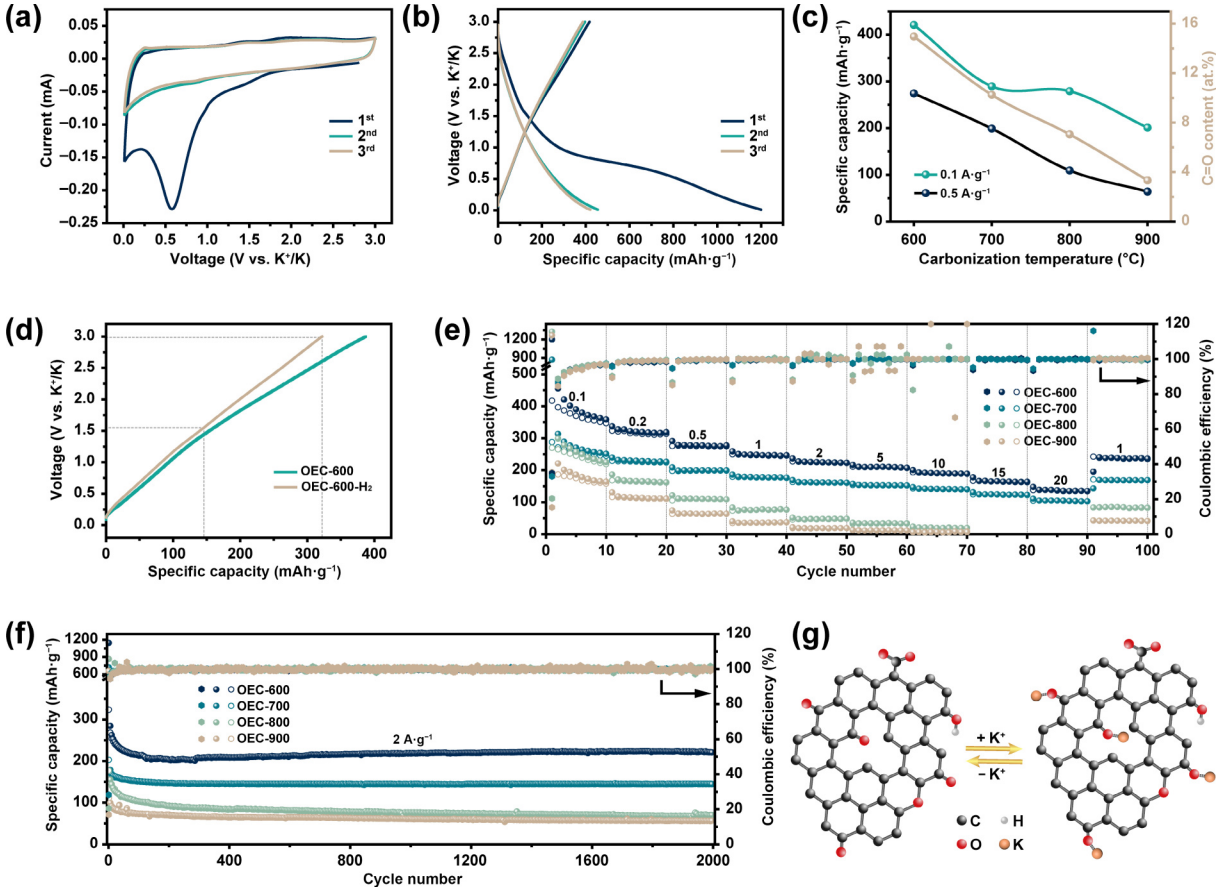


**Figure 3** Electrochemical properties of OEC-*x*. (a) CV curves of the first three cycles at 0.1 $mV{\cdot}s^{-1}$; (b) GCD curves of the first three cycles at 0.1 $A{\cdot}g^{-1}$ of OEC-600. (c) The relationship between specific capacity, C=O content and pyrolysis temperature. (d) The third cycle charge curves of OEC-600 and OEC-600-$H_2$ at 0.1 $A{\cdot}g^{-1}$. (e) Rate capability; (f) cycling stability at 2 $A{\cdot}g^{-1}$ of OEC-*x*. (g) Schematic illustration of energy storage mechanism of C=O.

cycling stability to various reported carbon anodes (Table S2 in the ESM). Moreover, to identify the optimal precursor component, the sodium storage capability of samples based on different precursor components was evaluated. As shown in Figs. S15 and S16 in the ESM, OEC-600 obtained from the precursor with $m$(EGCG)/$m$($CaCO_3$) = 1 exhibits optimal sodium storage capability.

A comprehensive kinetics analysis was performed to reveal the nature of the competitive fast-charging potassium storage capability of OEC-600. First, according to the equation of $i = k_1v + k_2v^{1/2}$ ($i$ is the current response at a chosen voltage, $v$ is the scan rate, $k_1$ and $k_2$ are constants), the CV curves of OEC-600 at different scan rates (Fig. S17(a) in the ESM) were fitted to quantify the contribution of capacitive-behavior and battery-behavior [40]. The fitting results are shown in Fig. S17(c) in the ESM, revealing a gradual rise in capacitive-behavior content as the scan rate increases. Obviously, the high content of capacitive-behavior (C=O dominant reversible potassium storage) with fast kinetics is the source of the attractive fast-charging potassium storage capability of OEC-600. Second, the $K^+$ diffusion coefficient ($D_k$) of OEC-600 was estimated by galvanostatic intermittent titration measurement. As presented in Fig. S18 in the ESM, the calculated $D_k$ of OEC-600 ranges from 3.2 × $10^{-12}$ to 2.5 × $10^{-11}$ $cm^2 \cdot s^{-1}$, which proves the superiority of $K^+$ diffusion in OEC-600. Finally, *in-situ* EIS was performed to analyze the evolution details of the potassium storage kinetics of OEC-600. As can be seen in Fig. 4(a), all Nyquist plots of the initial cycle of OEC-600 at 0.1 $mV \cdot s^{-1}$ are composed of two segments: One fragment is a semicircle in the high-frequency region, attributed to the diffusion resistance of $K^+$ at the interface of OEC-600 ($R_{SEI}$); another segment is a slope segment in the low-frequency region, assigned to the transfer resistance of $K^+$ in the bulk of OEC-600 ($R_d$) [41, 42]. Figure 4(b) summarized the $R_{SEI}$ (cyan line) of OEC-600 at different potassiation/depotassiation stages. At the potassiation stage, $R_{SEI}$ shrinks as the deepening of potassiation, which is attributed to the continuous formation of the SEI layer; at the subsequent depotassiation stage, a relatively stable $R_{SEI}$ can be observed, which is evidence that a stable SEI layer with high ionic conductivity has been generated at the interface of OEC-600. In addition, there is an anomalous jump in $R_{SEI}$ at the initial depotassiation stage. To explain this phenomenon, *ex-situ* high resolution TEM was tested. Surprisingly, dispersed potassium clusters can be observed in the fully discharged OEC-600 (Fig. 4(c)) and these potassium clusters disappear after full charge (Fig. 4(d)). It reveals that the abnormal jump of $R_{SEI}$ at the initial depotassiation stage is ascribed to the reversible oxidation of potassium clusters. Warburg coefficient (Fig. S19 in the ESM) was calculated to evaluate $R_d$. As shown in Fig. 4(b), the Warburg coefficient of OEC-600 (brown line) is highly reversible at the initial cycle, indicating that OEC-600 has extraordinary potassium storage reversibility.

Moreover, theoretical calculations were conducted to understand the effectiveness of C=O. The ESP mappings of the pure carbon model and the C=O doped carbon model are illustrated in Figs. 4(e) and 4(f). It can be observed that the C=O doped carbon model exhibits an uneven ESP distribution as compared with the pure carbon model, suggesting the charge polarization resulting from C=O doping. More importantly, in the C=O doped carbon model, the ESP minimum is distributed near the C=O, which demonstrates that $K^+$ is preferred to be stored at the C=O site. The deconvolution K 2p spectra of OEC-600 at different discharge states are shown in Fig. S20 in the ESM, where the significant K–O content is attributed to the reversible potassium storage of OFGs (represented by C=O). Furthermore, as shown in Fig. 4(g) and Fig. S21 in the ESM, *in-situ* Raman was tested to investigate the potassium storage reversibility of OEC-600. With the deepening of

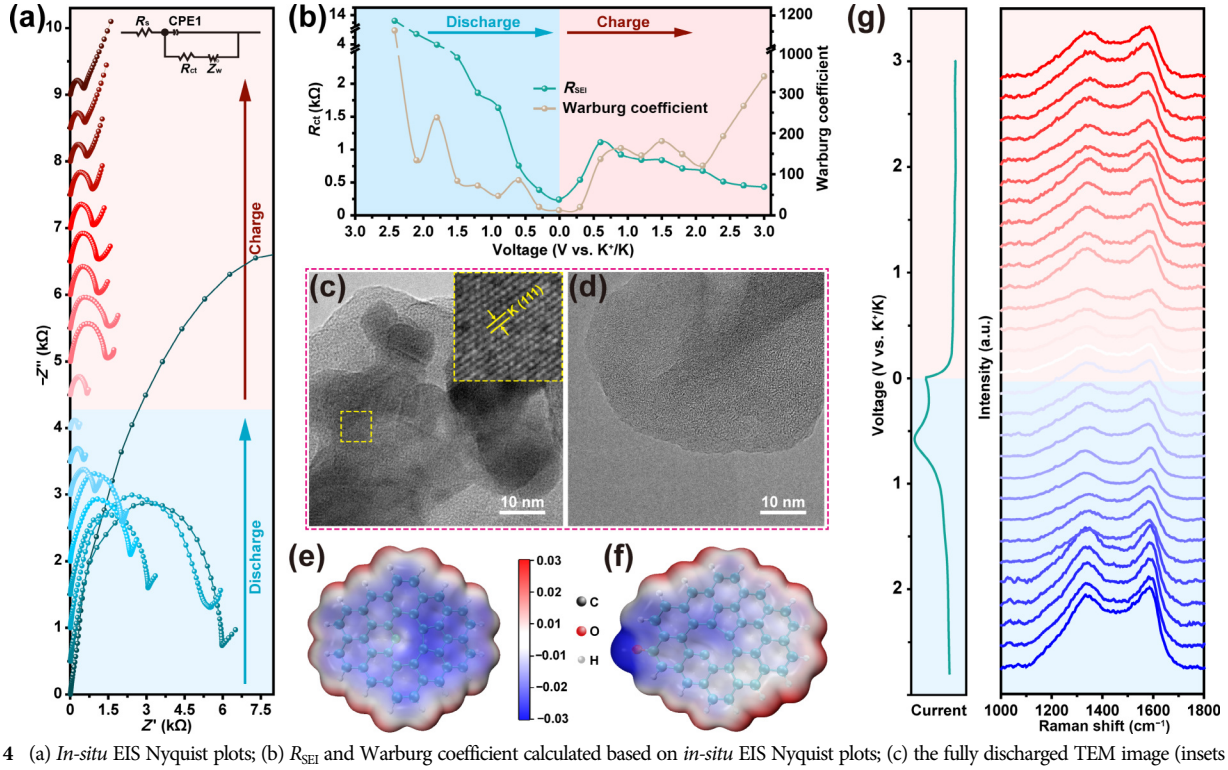


**Figure 4** (a) *In-situ* EIS Nyquist plots; (b) $R_{SEI}$ and Warburg coefficient calculated based on *in-situ* EIS Nyquist plots; (c) the fully discharged TEM image (insets are the calculated interlayer spacing and enlarged image of the yellow dotted rectangular area); (d) the fully charged TEM image of OEC-600. ESP images of (e) defect carbon; (f) oxygen-enriched carbon. (g) *In-situ* Raman spectra and corresponding CV curve at 0.2 $mV \cdot s^{-1}$ of OEC-600.

potassiation, the bands of OEC-600 present an evolutionary trend of first decline and then stability. Subsequently, this trend is reversed in the depotassiation stage. This phenomenon determines the excellent potassium storage reversibility of OEC-600. In addition, a slight shrinkage of the bands of OEC-600 can be observed after the initial cycle, which may result from the irreversible transformation of the structure of OEC-600.

To further evaluate the fast-charging potassium storage capability of OEC-600, a dual-carbon PIHC was constructed. An EGCG-based HPCS (Fig. S22 in the ESM) was selected as the cathode of PIHC. As shown in Fig. S23 and Table S3 in the ESM, HPCS is a micropore–mesopore hierarchical porous carbon with a specific surface area of up to 3462.6 ($m^2 \cdot g^{-1}$). As a potential cathode for PIHC (Fig. S24 in the ESM), HPCS presents 46 $mAh \cdot g^{-1}$ with an ultra-fast discharge time of 47.6 s at 15 $A \cdot g^{-1}$ and can cycle stably at 2 $A \cdot g^{-1}$. Depending on the operating voltage of the OEC-600 anode and HPCS cathode, the operating voltage of PIHC is determined to be 0.01–4 V (Fig. 5(a)). In addition, PIHCs with different mass ratios of HPCS to OEC-600 were assembled to obtain optimal potassium storage performance. As displayed in Fig. S25 in the ESM, PIHC-1.5 exhibits optimal comprehensive performance, so the mass ratio of HPCS to OEC-600 is determined to be 1.5: 1.

Figure S26 in the ESM illustrates the CV curves of PIHC-1.5, where the CV curves from 1 to 500 $mV \cdot s^{-1}$ exhibit similar profiles without significant distortion, revealing the superior potassium storage kinetics of PIHC-1.5. Further, as shown in the GCD curves (Fig. 5(b)), PIHC-1.5 has a high reversible specific capacity of 82.7 $mAh \cdot g^{-1}$ at 0.5 $A \cdot g^{-1}$ (the discharge time is 9.92 min) and it still maintains 40 $mAh \cdot g^{-1}$ of the specific capacity at 30 $A \cdot g^{-1}$ with an instantaneous discharge time of 4.8 s. Notably, not only the extraordinary reversible specific capacity, but also the *IR* drop (deviation due to current (*I*) and resistance (*R*)) of PIHC-1.5 is slight at the corresponding current density. As a consequence, PIHC-1.5 exhibits an ultra-high energy density of 145.1 $Wh \cdot kg^{-1}$ at a power density of 0.878 $kW \cdot kg^{-1}$ and outputs an outstanding energy density of 61.2 $Wh \cdot kg^{-1}$ at an ultra-high power density of 45.9 $kW \cdot kg^{-1}$, far superior to most recently reported PIHC (Fig. 5(d)) [17, 20, 43–50]. As for the fast-charging cycling stability, the PIHC-1.5 offers an impressive cycling stability with a capacity retention of 87.5% over 20,000 cycles at 5 $A \cdot g^{-1}$ and the capacity degradation per cycle is as low as 0.000625%. The above results display an impressive PIHC-1.5 with ultra-high fast-charging energy/power and ultra-long fast-charging cycling stability, demonstrating the bright prospects of OEC-600 in fast-charging PIHC devices.

## 4 Conclusions

In summary, we have successfully synthesized OEC with enhanced potassium storage kinetics and specific capacity based on epigallocatechin gallate precursor. The obtained amorphous OEC has a hierarchical porous structure and a tunable C=O content. In the K-half cells, OEC-600 with the highest C=O exhibits a reversible specific capacity of 417.5 $mAh \cdot g^{-1}$ at 0.1 $A \cdot g^{-1}$, achieves 135.2 $mAh \cdot g^{-1}$ with a discharge time of 27 s at a fast-charging current density of 20 $A \cdot g^{-1}$ and demonstrates a stable cycling stability at 2 $A \cdot g^{-1}$. Theoretical calculations and comprehensive kinetics analysis reveals the positive effects of C=O on the potassium storage kinetics and slope capacity of OEC-600 and *in-situ* Raman ascertains the excellent potassium storage reversibility of OEC-600. As a demonstration, the PIHCs assembled based on OEC-600 anode have impressive fast-charging performance. Specifically, the PIHCs deliver an ultra-high energy density of 145.1 $Wh \cdot kg^{-1}$ at 0.878 $kW \cdot kg^{-1}$ and output 61.2 $Wh \cdot kg^{-1}$ at an extremely high power density of 45.9 $kW \cdot kg^{-1}$. Moreover, at a fast-charging current density of 5 $A \cdot g^{-1}$, the capacity retention of PIHCs after 20,000 cycles is up to 87.5% (0.000625% capacity degradation per cycle). We believe this work is anticipated to provide an optional design concept toward the carbon anode for fast-charging PIHCs.

**Electronic Supplementary Material**: Supplementary material (FTIR spectra, SEM and TEM images, TG-derivative thermogravimetric analysis (DTG)-differential scanning calorimetry (DSC) curves, XPS spectra, $N_2$ adsorption–desorption measurements, electrochemical properties and *in-situ* Raman

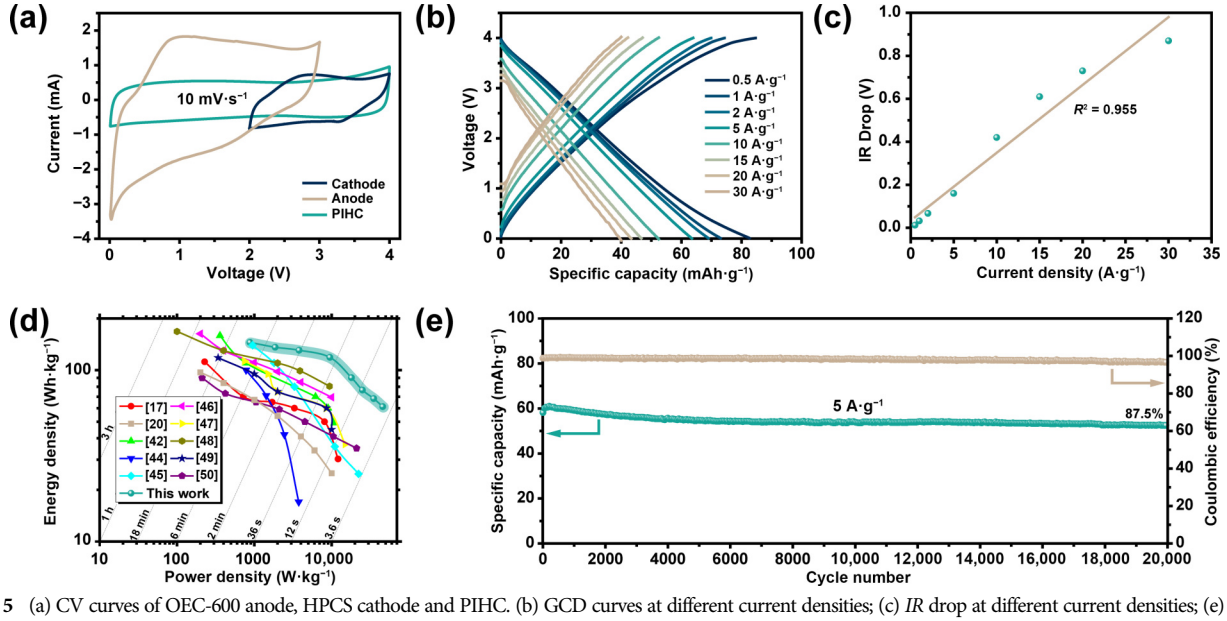


**Figure 5** (a) CV curves of OEC-600 anode, HPCS cathode and PIHC. (b) GCD curves at different current densities; (c) *IR* drop at different current densities; (e) cycling stability at 5 $A \cdot g^{-1}$ of PIHC. (d) Ragone plots in comparison with other works.

spectra) is available in the online version of this article at https://doi.org/10.26599/NR.2025.94907033.

## Data availability

All data needed to support the conclusions in the paper are presented in the manuscript and the Electronic Supplementary Material. Additional data related to this paper may be requested from the corresponding author upon request.

## Acknowledgements

This work was financially supported by the National Key R&D Program of China (No. 2022YFB3807700), the National Natural Science Foundation of China (Nos. 52072217, 22179071, U20A20337, 52130206 and 52402278), the Hubei Natural Science Foundation Innovation Group Project (No. 2022CFA020), Joint Funds of the Hubei Natural Science Foundation Innovation and Development (No. 2022CFD034), the Yichang Natural Science Research Project (No. A24-3-013) and the Science Foundation of China Three Gorges University (No. 2023RCKJ0021).

## Declaration of competing interest

All the contributing authors report no conflict of interests in this work.

## Author contribution statement

D. P. Q.: Writing – original draft, writing – review & editing, visualization, validation, software, methodology, investigation, formal analysis, data curation, conceptualization. Y. H. W.: Writing – original draft, validation, formal analysis, data curation. L. L. Z.: Writing – review & editing, formal analysis. H. L.: Formal analysis. H. Z. Y.: Formal analysis. J. N.: Formal analysis. M. L.: Formal analysis. X. L. Y.: Writing – review & editing, supervision, project administration, resources, investigation, formal analysis, conceptualization. F. W.: Writing – review & editing, supervision, project administration, resources, investigation, formal analysis. R. Y.: Writing – review & editing, supervision, project administration, investigation, formal analysis. All the authors have approved the final manuscript.

## Use of AI statement

None.

## References

[1] Gervillié-Mouravieff, C.; Boussard-Plédel, C.; Huang, J. Q.; Leau, C.; Blanquer, L. A.; Yahia, M. B.; Doublet, M. L.; Boles, S. T.; Zhang, X. H.; Adam, J. L. et al. Unlocking cell chemistry evolution with *operando* fibre optic infrared spectroscopy in commercial Na(Li)-ion batteries. *Nat. Energy* **2022**, *7*, 1157–1169.

[2] Paul, P. P.; Thampy, V.; Cao, C. T.; Steinrück, H. G.; Tanim, T. R.; Dunlop, A. R.; Dufek, E. J.; Trask, S. E.; Jansen, A. N.; Toney, M. F. et al. Quantification of heterogeneous, irreversible lithium plating in extreme fast charging of lithium-ion batteries. *Energy Environ. Sci.* **2021**, *14*, 4979–4988.

[3] Tu, S. B.; Zhang, B.; Zhang, Y.; Chen, Z. H.; Wang, X. C.; Zhan, R. M.; Ou, Y. T.; Wang, W. Y.; Liu, X. R.; Duan, X. R. et al. Fast-charging capability of graphite-based lithium-ion batteries enabled by $Li_3P$-based crystalline solid–electrolyte interphase. *Nat. Energy* **2023**, *8*, 1365–1374.

[4] Li, Y. Q.; Vasileiadis, A.; Zhou, Q.; Lu, Y. X.; Meng, Q. S.; Li, Y.; Ombrini, P.; Zhao, J. B.; Chen, Z.; Niu, Y. S. et al. Origin of fast charging in hard carbon anodes. *Nat. Energy* **2024**, *9*, 134–142.

[5] Wang, R.; Wang, L.; Liu, R.; Li, X. Y.; Wu, Y. Z.; Ran, F. "Fast-charging" anode materials for lithium-ion batteries from perspective of ion diffusion in crystal structure. *ACS Nano* **2024**, *18*, 2611–2648.

[6] Rudola, A.; Sayers, R.; Wright, C. J.; Barker, J. Opportunities for moderate-range electric vehicles using sustainable sodium-ion batteries. *Nat. Energy* **2023**, *8*, 215–218.

[7] Sun, C. C.; Ji, X.; Weng, S. T.; Li, R. H.; Huang, X. T.; Zhu, C. N.; Xiao, X. Z.; Deng, T.; Fan, L. W.; Chen, L. X. et al. 50C fast-charge Li-ion batteries using a graphite anode. *Adv. Mater.* **2022**, *34*, 2206020.

[8] Lu, L. L.; Lu, Y. Y.; Zhu, Z. X.; Shao, J. X.; Yao, H. B.; Wang, S. G.; Zhang, T. W.; Ni, Y.; Wang, X. X.; Yu, S. H. Extremely fast-charging lithium ion battery enabled by dual-gradient structure design. *Sci. Adv.* **2022**, *8*, eabm6624.

[9] Zhao, W. Q.; Lei, S. Y.; Li, J. X.; Jiang, F.; Wu, T. J.; Yang, Y.; Sun, W.; Ji, X. B.; Ge, P. Modulating internal coordination configurations for high-density atomic antimony toward advanced fast-charging sodium-ion batteries. *Adv. Energy Mater.* **2024**, *14*, 2304431.

[10] Zhao, S. Q.; Li, G. H.; Zhang, B. H.; Li, T. M.; Luo, M. C.; Sun, B.; Wang, G. X.; Guo, S. J. Technological roadmap for potassium-ion hybrid capacitors. *Joule* **2024**, *8*, 922–943.

[11] Cai, P.; Wang, K. L.; Wang, T. Q.; Li, H. M.; Zhou, M.; Wang, W.; Jiang, K. Comprehensive insights into potassium-ion capacitors: Mechanisms, materials, devices and future perspectives. *Adv. Energy Mater.* **2024**, *14*, 2401183.

[12] Le Comte, A.; Reynier, Y.; Vincens, C.; Leys, C.; Azaïs, P. First prototypes of hybrid potassium-ion capacitor (KIC): An innovative, cost-effective energy storage technology for transportation applications. *J. Power Sources* **2017**, *363*, 34–43.

[13] Liu, X.; Elia, G. A.; Qin, B. S.; Zhang, H.; Ruschhaupt, P.; Fang, S.; Varzi, A.; Passerini, S. High-power Na-ion and K-ion hybrid capacitors exploiting cointercalation in graphite negative electrodes. *ACS Energy Lett.* **2019**, *4*, 2675–2682.

[14] Li, H. X.; Gong, Y.; Zhou, H. H.; Li, J.; Yang, K.; Mao, B. Y.; Zhang, J. C.; Shi, Y.; Deng, J. H.; Mao, M. X. et al. Ampere-hour-scale soft-package potassium-ion hybrid capacitors enabling 6-minute fast-charging. *Nat. Commun.* **2023**, *14*, 6407.

[15] Qiu, D. P.; Guan, J. Y.; Li, M.; Kang, C. H.; Wei, J. Y.; Li, Y.; Xie, Z. Y.; Wang, F.; Yang, R. Kinetics enhanced nitrogen-doped hierarchical porous hollow carbon spheres boosting advanced potassium-ion hybrid capacitors. *Adv. Funct. Mater.* **2019**, *29*, 1903496.

[16] Liu, Z. Y.; Peng, H.; Xie, X.; Wang, X.; Hou, W. B.; Miao, W. X.; Tao, B.; Ma, G. F.; Lei, Z. Q. Coupling of reasonable micro-defect structure and multiple chemisorption sites for boosting the $K^+$ storage capacity in dual-carbon potassium ion hybrid capacitors. *Energy Storage Mater.* **2024**, *65*, 103100.

[17] Yu, L.; He, X. Y.; Peng, B.; Wang, W. T.; Wan, G. L.; Ma, X. Y.; Zeng, S. Y.; Zhang, G. Q. Constructing ion diffusion highway in strongly coupled $WSe_2$-carbon hybrids enables superior energy storage performance. *Matter* **2023**, *6*, 1604–1621.

[18] Liu, S. D.; Kang, L.; Zhang, J.; Jun, S. C.; Yamauchi, Y. Carbonaceous anode materials for non-aqueous sodium- and potassium-ion hybrid capacitors. *ACS Energy Lett.* **2021**, *6*, 4127–4154.

[19] Lu, X. Y.; Zhou, J. J.; Huang, L.; Peng, H. D.; Xu, J. L.; Liu, G. P.; Shi, C. L.; Sun, Z. PP. Low-temperature carbonized N/O/S-tri-doped hard carbon for fast and stable K-ions storage. *Adv. Energy Mater.* **2024**, *14*, 2303081.

[20] Jiang, J. M.; Chen, Z. Y.; Chen, Y. X.; Zhuang, Q. C.; Ju, Z. C.; Zhang, X. G. Engineering local graphitic domains to balance defect active site and electronic conduction ability in coal-derived carbon anode for superior potassium ions storage. *Adv. Funct. Mater.* **2024**, *34*, 2402416.

[21] Yang, Y. H.; Zhou, J.; Rao, A. M.; Lu, B. A. Bio-inspired carbon electrodes for metal-ion batteries. *Nanoscale* **2024**, *16*, 5893–5902.

[22] Wu, L. C.; Fu, H. W.; Lyu, W.; Cha, L. M.; Rao, A. M.; Guo, K. K.;

Zhou, J.; Wen, S. C.; Lu, B. A. Rational regulation of high-voltage stability in potassium layered oxide cathodes. *ACS Nano* **2024**, *18*, 13415–13427.
[23] Qiu, D. P.; Hou, Y. L. Carbon materials toward efficient potassium storage: Rational design, performance evaluation and potassium storage mechanism. *Green Energy Environ.* **2023**, *8*, 115–140.
[24] Yuan, F.; Li, Y. N.; Wang, Y. Q.; Li, Z. J.; Wang, Q. J.; Sun, H. L.; Zhang, D.; Wang, W.; Wang, B. Cobalt nanoparticles synergize with oxygen-containing functional groups to realize fast and stable potassium storage for carbon anode. *Adv. Funct. Mater.* **2023**, *33*, 2304753.
[25] Deng, W. T.; Cao, Y. J.; Yuan, G. M.; Liu, G. G.; Zhang, X.; Xia, Y. Y. Realizing improved sodium-ion storage by introducing carbonyl groups and closed micropores into a biomass-derived hard carbon anode. *ACS Appl. Mater. Interfaces* **2021**, *13*, 47728–47739.
[26] Frisch, M. J.; Trucks, G. W.; Schlegel, H. B.; Scuseria, G. E.; Robb, M. A.; Cheeseman, J. R.; Scalmani, G.; Barone, V.; Petersson, G. A.; Nakatsuji, H. et al. *Gaussian 16*, Revision C.01; Gaussian Inc.: Wallingford, CT, USA, 2016.
[27] Lu, T.; Chen, F. W. Multiwfn: A multifunctional wavefunction analyzer. *J. Comput. Chem.* **2012**, *33*, 580–592.
[28] Krupkova, O.; Ferguson, S. J.; Wuertz-Kozak, K. Stability of (–)-epigallocatechin gallate and its activity in liquid formulations and delivery systems. *J. Nutr. Biochem.* **2016**, *37*, 1–12.
[29] Yan, Y.; Cui, Y. B.; Wang, Q. Y.; Che, Z. X.; Liu, T.; Li, A. R.; Zhou, W. Mg-doped $CaCO_3$ nanoarchitectures assembled by $(44\bar{1})$ high-index facets for efficient trace removal of Pb(II). *Rare Met.* **2023**, *42*, 525–535.
[30] Shahzadi, I.; Islam, M.; Saeed, H.; Shahzadi, A.; Haider, J.; Haider, A.; Imran, M.; Rathore, H. A.; Ul-Hamid, A.; Nabgan, W. et al. Facile synthesis of copolymerized cellulose grafted hydrogel doped calcium oxide nanocomposites with improved antioxidant activity for anti-arthritic and controlled release of doxorubicin for anti-cancer evaluation. *Int. J. Biol. Macromol.* **2023**, *235*, 123874.
[31] Hou, Z. D.; Jiang, M. W.; Lei, D.; Zhang, X.; Gao, Y. Y.; Wang, J. G. Regulation of pseudographitic carbon domain to boost sodium energy storage. *Nano Res.* **2024**, *17*, 5188–5196.
[32] Sadezky, A.; Muckenhuber, H.; Grothe, H.; Niessner, R.; Pöschl, U. Raman microspectroscopy of soot and related carbonaceous materials: Spectral analysis and structural information. *Carbon* **2005**, *43*, 1731–1742.
[33] Oh, J. A. S.; Deysher, G.; Ridley, P.; Chen, Y. T.; Cheng, D. Y.; Cronk, A.; Ham, S. Y.; Tan, D. H. S.; Jang, J.; Nguyen, L. H. B. et al. High-performing all-solid-state sodium-ion batteries enabled by the presodiation of hard carbon. *Adv. Energy Mater.* **2023**, *13*, 2300776.
[34] Qiu, D. P.; Zhao, W. T.; Zhang, B.; Ahsan, M. T.; Wang, Y. H.; Zhang, L. L.; Yang, X. L.; Hou, Y. L. Ni-single atoms modification enabled kinetics enhanced and ultra-stable hard carbon anode for sodium-ion batteries. *Adv. Energy Mater.* **2024**, *14*, 2400002.
[35] Zheng, Z.; Hu, S. J.; Yin, W. J.; Peng, J.; Wang, R.; Jin, J.; He, B. B.; Gong, Y. S.; Wang, H. W.; Fan, H. J. $CO_2$-etching creates abundant closed pores in hard carbon for high-plateau-capacity sodium storage. *Adv. Energy Mater.* **2024**, *14*, 2303064.
[36] Lian, J. B.; Subburam, G.; El-Khodary, S. A.; Zhang, K.; Zou, B. B.; Wang, J.; Wang, C.; Ma, J. M.; Wu, X. J. Critical role of aromatic C($sp^2$)–H in boosting lithium-ion storage. *J. Am. Chem. Soc.* **2024**, *146*, 8110–8119.
[37] Deng, H. L.; Wang, L.; Li, S. Y.; Zhang, M.; Wang, T.; Zhou, J.; Chen, M. X.; Chen, S.; Cao, J. H.; Zhang, Q. S. et al. Radial pores in nitrogen/oxygen dual-doped carbon nanospheres anode boost high-power and ultrastable potassium-ion batteries. *Adv. Funct. Mater.* **2021**, *31*, 2107246.
[38] Yue, W. C.; Yu, Z. S.; Man, Y.; Zhang, X. K.; Li, J. J.; Liu, H. Y.; Ma, X. Q. Synthesis of natural oxygen-doped bamboo-derived hierarchical micro-mesoporous composite carbon materials using a green activation strategy. *J. Energy Storage* **2024**, *90*, 111871.
[39] Barton, T. J.; Bull, L. M.; Klemperer, W. G.; Loy, D. A.; McEnaney, B.; Misono, M.; Monson, P. A.; Pez, G.; Scherer, G. W.; Vartuli, J. C. et al. Tailored porous materials. *Chem. Mater.* **1999**, *11*, 2633–2656.
[40] Kim, H. S.; Cook, J. B.; Lin, H.; Ko, J. S.; Tolbert, S. H.; Ozolins, V.; Dunn, B. Oxygen vacancies enhance pseudocapacitive charge storage properties of $MoO_{3-x}$. *Nat. Mater.* **2017**, *16*, 454–460.
[41] Zhang, M.; Liu, X. X.; Ji, T. Y.; Li, Y.; Sheng, D. W.; Li, S. D.; Ren, P. P.; Shen, Z. X. High-performance sodium storage for cobalt phosphide composite array electrodes. *Rare Met.* **2024**, *43*, 3724–3734.
[42] Zhang, Y. X.; Chen, Y. Z. Y.; Jiang, Y.; Wang, J.; Zheng, X. Y.; Han, B.; Xia, K. S.; Gao, Q.; Cai, Z.; Zhou, C. G. et al. Construction of $VS_2/VO_x$ heterostructure via hydrolysis-oxidation coupling reaction with superior sodium storage properties. *Adv. Funct. Mater.* **2023**, *33*, 2212785.
[43] Xu, C. R.; Mu, J. L.; Zhou, T.; Tian, S.; Gao, P. B.; Yin, G. C.; Zhou, J.; Li, F. Surface redox pseudocapacitance boosting vanadium nitride for high-power and ultra-stable potassium-ion capacitors. *Adv. Funct. Mater.* **2022**, *32*, 2206501.
[44] Xie, W.; Zhang, Q. F.; Song, S.; Cheng, X. L.; Yang, Y.; Wang, L. L.; Ouyang, X. P.; Xie, S. H.; Huang, J. Y. High S-doped amorphous carbon/carbon quantum dots coupled micro-frame for highly efficient potassium storage. *J. Colloid Interface Sci.* **2023**, *652*, 1522–1532.
[45] Zhang, B. C.; Liu, S.; Li, H. C.; Wang, D.; Kang, W. P.; Sun, D. F. Confined assembly of hydrated vanadium oxide into hollow mesoporous carbon nanospheres for fast and stable $K^+$ storage capability. *Small* **2023**, *19*, 2208228.
[46] Xu, Y. F.; Li, Y. H.; Wang, T. S.; Liu, Q. S.; Fang, X. R.; Ding, X. T.; Chen, Z. Y.; Zhang, C. L.; Niu, H. T.; Zhou, H. et al. Dual strategies of interface engineering and core–shell structure improve potassium storage performance. *Chem. Eng. J.* **2024**, *479*, 147848.
[47] Xiong, Y.; Zhang, Y. F.; Zhu, C. L.; Yang, L.; Liang, H. Y.; Shi, J.; Chen, J. W.; Tian, W. Q.; Liu, S.; Li, Z. et al. Carbon cathode with heteroatom doping and ultrahigh surface area enabling enhanced capacitive behavior for potassium-ion hybrid capacitors. *Rare Met.* **2024**, *43*, 2136–2149.
[48] Wang, K. F.; Sun, F.; Zhang, B. R.; Wu, D. Y.; Wang, H.; Gao, J. H.; Zhao, G. B. Nitrogen-doped hollow carbon nanoparticles with optimized multiscale nanostructures via dolomite-assisted chemical vapor deposition for high-performance potassium-ion capacitor. *Carbon* **2023**, *214*, 118318.
[49] Ouyang, Y. J.; Li, P.; Ma, Y.; Wei, J. W.; Tian, W. Q.; Chen, J. W.; Shi, J.; Zhu, Y.; Wu, J. Y.; Wang, H. L. Thermal induced conversion of CoFe prussian blue analogs nanocubes wrapped by doped carbon network exhibiting fast and stable potassium ion storage as anode. *Small* **2024**, *20*, 2308484.
[50] Zhong, L.; Qiu, X. Q.; Yang, S. S.; Sun, S. R.; Chen, L. H.; Zhang, W. L. Supermolecule-regulated synthesis strategy of general biomass-derived highly nitrogen-doped carbons toward potassium-ion hybrid capacitors with enhanced performances. *Energy Storage Mater.* **2023**, *61*, 102887.